Commissioning of a photoelectron spectrometer for soft X-ray photon diagnostics at the European XFEL[1]

Joakim Laksman,[a]* Jens Buck,[b,c] Leif Glaser,[b] Marc Planas,[a] Florian Dietrich,[a] Jia Liu,[a] Theophilos Maltezopoulos,[a] Frank Scholz,[b] Jörn Seltmann,[b] Gregor Hartmann,[b,d] Markus Ilchen,[a,d] Wolfgang Freund,[a] Naresh Kujala,[a] Jens Viefhaus[b,e] and Jan Grünert[a]

[a]European XFEL, Holzkoppel 4, 22869 Schenefeld, Germany, [b]Deutsches Elektronen-Synchrotron DESY, Notkestraße 85, 22607 Hamburg, Germany, [c]Christian-Albrechts-Universität zu Kiel, Institut für Experimentelle und Angewandte Physik, Leibnizstraße 19, 24098 Kiel, Germany, [d]Institut für Physik, University of Kassel, Heinrich-Plett-Straße 40, 34132 Kassel, Germany, and [e]Helmholtz-Zentrum Berlin für Materialien und Energie, Berlin, Germany.
*Correspondence e-mail: joakim.laksman@xfel.eu

Commissioning and first operation of an angle-resolved photoelectron spectrometer for non-invasive shot-to-shot diagnostics at the European XFEL soft X-ray beamline are described. The objective with the instrument is to provide the users and operators with reliable pulse-resolved information regarding photon energy and polarization that opens up a variety of applications for novel experiments but also hardware optimization.

1. Introduction

The principle of linear-accelerator-based self-amplification of spontaneous emission (SASE) is that a collimated electron bunch is accelerated to almost the speed of light prior to injection in a periodic magnetic field undulator where electromagnetic radiation is generated. Spatial modulation of electron bunches takes place as they interact with the electromagnetic field leading them to ultimately radiate in phase and producing highly coherent and intense X-ray pulses (Pellegrini *et al.*, 2016). The unique properties of X-ray free-electron laser (XFEL) radiation with high intensity (up to $\sim 10^{12}$ photons pulse^{-1}), high repetition rate and short pulse length (1–100 fs) has found applications in physics, chemistry, biology and medicine where the ability to take snapshots of samples on a molecular length and time scale provides a wealth of new information. The construction of XFEL facilities around the world has created a need for instrumentation development for diagnostics and data acquisition that is capable of handling these requirements without damage or being overloaded but at the same time provide relevant beam parameters (Ullrich *et al.*, 2012; Feldhaus *et al.*, 2013; Yabashi *et al.*, 2013; Bostedt *et al.*, 2016; Seddon *et al.*, 2017; Kraus *et al.*, 2018).

At the European XFEL (EuXFEL) facility in Schenefeld, Germany, the X-ray photon diagnostics group (XPD) utilizes a large array of techniques for providing beam parameters to users and operators (Grünert *et al.*, 2019; Tschentscher *et al.*, 2017). A non-invasive principle for photon diagnostics is the usage of low-density matter where gas targets are ionized by XFEL pulses and only the resulting ions or electrons are detected (Braune *et al.*, 2016). Two complementary gas-based devices that provide pulse-resolved information are (i) the X-ray gas monitor (XGM), that monitors beam position and
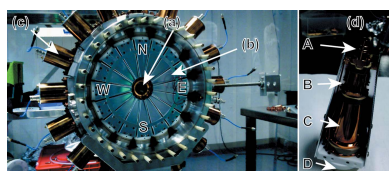
absolute pulse energy (Tiedtke *et al.*, 2009; Maltezopoulos *et al.*, 2019), and (ii) the photoelectron spectrometer (PES), that measures spectral distribution and polarization.

In this paper we describe the PES instrument for diagnostics installed in the SASE3 beamline. It is located in tunnel XTD10 (3142 m from the injector) downstream of the XGM and upstream of the gas-attenuator (GATT), horizontal offset mirrors (HOMS) and the monochromator. The location is chosen to provide better feedback for FEL control to know in which direction the photon energy deviates in shots where it is not matching the monochromator. The beamline with variable-gap undulators can provide soft X-rays in the range 250–3000 eV to the scientific endstations Small Quantum Systems (SQS) and Spectroscopy and Coherent Scattering (SCS). At the moment only horizontal polarization is possible, but, with the future installation of an afterburner (Lutman *et al.*, 2016), circular and elliptical polarization will be provided to the users.

SASE is a stochastic process where pulses have individual characteristics. The purpose of this instrument is, accordingly, to provide machine operators and users with shot-to-shot information about the photon energy spectrum and the polarization. This has a wide range of applications: experiments at resonances where narrow and precise bandwidth is crucial will use the monochromator to select their desired photon energy, but they will rely on precise undulator tuning which can only be achieved with the non-invasive diagnostics that the PES provides (Braune *et al.*, 2018). Studies of magnetic material properties and circular dichroism will require full polarization control and monitoring of the Stokes parameters. Objectives for the PES instrument are defined by the user requirements which are relative photon energy resolution of 10^{-3} to 10^{-4} and determination of the X-ray polarization vector with 1% accuracy. These values must be supplied to operators for efficient tuning of the undulator gap and the future afterburner. In addition, they must be collected and stored in the same data file as the user experiment for cross correlation and data sorting. An additional application of the PES that will be implemented in SASE3 is to send the evaluated center wavelength to the XGM DOOCS server for cross checking with the value taken from the undulator server. Furthermore, due to data transfer capacity limitations, 2D pixelated imaging detectors at the endstations can currently process and store data from only up to 800 of the 2700 pulses that are potentially available from the machine within one pulse train. To optimize the amount of useful data, a veto system is being implemented at EuXFEL. Whenever the PES encounters a pulse with undesired photon energy and/or polarization, a signal is sent to the imaging detector, prompting it to overwrite the data of this recorded pulse with later pulses from the same pulse train.

With this routine, we ensure that as much as possible of the storage capacity indeed contain high-quality data.

2. Instrument

Electron spectrometers based on the time-of-flight (TOF) concept have drift-tubes with tunable voltages that decelerate the electrons. Fast electronics register the time difference from ionization to detection which is related to the kinetic energy of the photoelectrons. The PES presented here is based on a design made originally for the online diagnostic unit of beamline P04 at PETRA III, DESY, Hamburg, Germany (Viefhaus *et al.*, 2013), which has previously been operated at several FEL facilities and proven itself as a versatile tool for photon diagnostics (Allaria *et al.*, 2014; Ferrari *et al.*, 2015; Hartmann *et al.*, 2016; Roussel *et al.*, 2017; von Korff Schmizing *et al.*, 2017), angular streaking (Düsterer *et al.*, 2016; Hartmann *et al.*, 2018) as well as molecular and multi-photon physics (Ilchen *et al.*, 2012, 2018). To achieve angular photoemission resolution with respect to the polar angle, the PES consists of 16 electron TOF spectrometers oriented perpendicular to the X-ray beam (see Fig. 1). The drift-tubes of the EuXFEL PES are labeled [*N NNE NE ENE E* . . .], where *N* and *S* are positioned vertical while *E* and *W* are positioned horizontal, left and right, respectively, seen from upstream. An advantage of having 16 spectrometers is the high redundancy that results, for example, for low-energy pulses or photon energy regions with low cross-section. More reliable spectral data can be retrieved by summing different channels together achieving higher single-pulse statistics.

In the case of the EuXFEL PES a target gas which can be a rare gas (Ne, Kr or Xe) or N_2 is injected as an effusive jet in the interaction region center via a 100 µm inner-diameter capillary. Reference data for the gas targets can be found for cross sections (Yeh & Lindau, 1985), the anisotropy parameter (Derevianko *et al.*, 1999; Lindle *et al.*, 1984), binding energy (Cardona & Ley, 1978) and linewidth (Prince *et al.*, 1999). The four gas targets available for the PES inside the EuXFEL
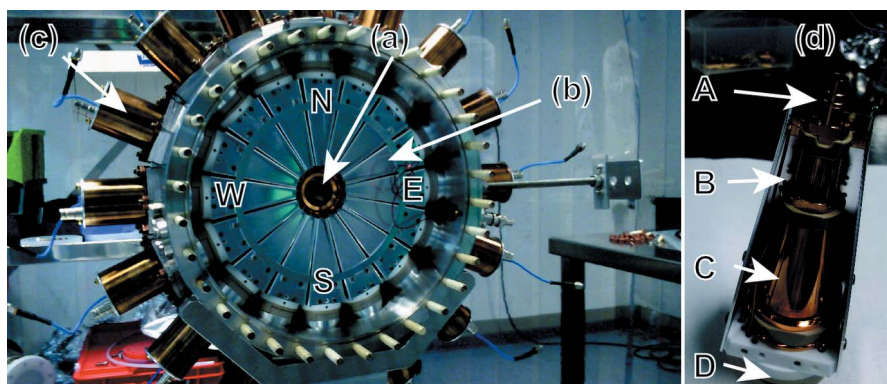
Figure 1
Photoelectron spectrometer assembled in the dedicated vacuum chamber. (*a*) In the interaction region, EuXFEL pulses ionize the effusive gas target which is injected via a capillary. (*b*) 16 electron TOF drift-tubes provides polar angular resolution. (*c*) Each detector is mounted on a separate flange with feedthroughs for high voltage and signal readout. (*d*) Drift-tube with shield partially disassembled to display the four segments [A B C D].

Table 1
Photoemission lines for available gas targets.

Orbital	Photoelectron binding energy (eV)†			
	N2	Ne	Kr	Xe
K 1s	409.9	870.2	14326	34561
L_1 2s	37.3	48.5	1921	5453
L_2 $2p_{1/2}$	11.5	21.7	1730.9	5107
L_3 $2p_{3/2}$	11.5	21.6	1678.4	4786
M_1 3s			292.8	1148.7
M_2 $3p_{1/2}$			222.2	1002.1
M_3 $3p_{3/2}$			214.4	940.6
M_4 $3d_{3/2}$			95.0	689.0
M_5 $3d_{5/2}$			93.8	676.4
N_1 4s			27.5	213.2
N_2 $4p_{1/2}$			14.1	146.7
N_3 $4p_{3/2}$			14.1	145.5
N_4 $4d_{3/2}$				69.5
N_5 $4d_{5/2}$				67.5
O_1 5s				23.4
O_2 $5p_{1/2}$				13.4
O_3 $5p_{3/2}$				12.1

† Values taken from Cardona & Ley (1978).

tunnel are selected with the motivation of covering the entire soft X-ray region 250–3000 eV at SASE3. The criteria are: (i) sufficient cross section for single-shot diagnostics; (ii) low kinetic energy of the created photoelectrons to achieve good photon energy resolution; (iii) anisotropy parameter β far from 0 to retrieve reliable polarization; (iv) avoid overlap with Auger lines that would make the data unreliable. For example, around 900 eV, the best choice is Ne 1s (see Table 1) with a binding energy of 870.2 eV. At this photon energy, the cross section is $\sigma > 0.2$ Mb, $\beta = 2.00$ and the KLL Auger lines do not overlap with the photoline. The base pressure in the chamber is 1×10^{-8} mbar. Depending on the ionization cross section we inject gas to a background pressure of 1×10^{-7} to 1×10^{-5} mbar. An X-ray pulse ionizes the target and photoelectrons are ejected anisotropically whereof a small fraction are registered by the detectors from which linear momentum data can be deduced.

The drift-tubes are each composed of four conical electrode segments constructed of copper beryllium where we apply voltages to decelerate the electrons. The segments are labeled [A B C D] in Fig. 1. The total distance from the central symmetry interaction point to the detector is 135 mm. The entrance hole of a drift-tube has a diameter of 3 mm. The acceptance angle for each spectrometer is 0.2% of 4π. The PES is located far from any focus and the beam spot size is estimated to be about 5 mm in diameter. Deceleration voltages are selected for optimizing TOF resolution and focusing electrons to the detector for optimal transmission. In general we operate with the settings $R \times [0.00\ 0.65\ 0.90\ 1.00]$, where the lowest voltage is closest to the interaction region and the highest voltage is closest to the detector. The deceleration settings can be described with the retardation value R. We have empirically and from simulations found this potential gradient to optimize the performance. In general the kinetic energy must be reduced to about 15–60 eV in order to achieve sufficient resolution (Buck, 2012). Each drift-tube is enclosed

with grounded aluminium sheet metal for electromagnetic shielding from the surrounding environment. Detectors are Z-stack MCPs (Hamamatsu F1552-011) with an in-house designed assembly with anodes and electronics made by the P04 group at DESY, Hamburg. A grid mesh is placed in front of the MCP stack with the same voltage as the last segment for creating a post-acceleration region near the detector to increase detection efficiency.

Data acquisition is performed with four digitizer boards (SP Devices ADQ 412-4G) in a µTCA crate that we operate in four-channel mode with 2 GS s^{-1} (500 ps binning). An option is to bridge two channels in order to increase the sample rate to 4 GS s^{-1} (250 ps binning). Their dynamic range is ± 400 mV. Prior to digitizers we use pre-amplifiers (Mini-circuits ZFL-1000LN+) that enhance the MCP-detector signal and also protect the expensive digitizer channels from possible overvoltages exceeding their maximum allowed value of ± 1 V. For additional signal matching, the signal chain contains 3 dB attenuators at the input of the pre-amplifiers and 10 dB attenuators at the input of the digitizers. A 3D Helmholtz coil structure encloses the device and is used to cancel out the background magnetic field which otherwise would influence the electron trajectories. A fluxgate-type magnetometer (Bartington Mag-03) is mounted to the vacuum chamber to monitor the magnetic field. The required voltages for PES electrodes, MCP detectors, pre-amplifiers and Helmholtz coils are applied with a modular high-voltage supply (MPOD). For alignment of the instrument to the beam the setup has decoupled translation and rotation motion in all six degrees of freedom controlled by stepper motors. Six fiducials are placed on the chamber to enable pre-alignment by a laser tracker. Stepper motors, magnetometer, pumps, gate valves and pressure gauges are connected via a crate with Beckhoff modules for power and readout. MPOD, µTCA and Beckhoff crates are remotely operated via the Karabo control system which is a SCADA environment designed for both hardware control and data acquisition (Hauf, 2019).

Fig. 2 presents a functional scheme of the control and data acquisition system. The plotted voltage signal shows a typical spectrum where the first peak is the prompt from scattered light and the following peaks result from photoelectrons. The time difference gives us the TOF if we add the 0.45 ns it takes for the light propagation from the interaction region to the detector. In general the external trigger given from the bunch pattern is stable within the time frame of an experiment so no new readout of the prompt is required to define a reference TOF.
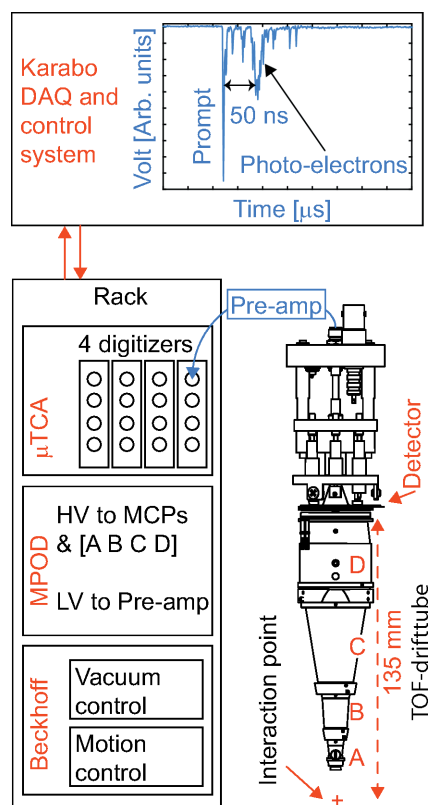
3. Results

3.1. Spectral distribution

The photoelectron's kinetic energy E_K can be written as

$$E_K = \frac{m_e L^2}{2T^2},\tag{1}$$

where m_e is the electron mass, L is the distance the electrons travel and T is the TOF. Indeed, for 0 V retardation where no

Figure 2
Functional scheme of data acquisition and control system. Vacuum components and stepper motors are controlled via Beckhoff terminals. Voltages for drift-tube segments [A B C D], detectors, amplifiers and Helmholtz coils are supplied via an MPOD crate. The detector signal is, after amplification, read by digitizers in a μTCA crate. The presented plot is a typical single-pulse spectrum where the first peak is the prompt from scattered light and the following peak is from photoelectrons. The rack containing all the electronics is remotely operated via the Karabo control system which is an environment designed for hardware control and data acquisition.

electric field penetration is present, the electron TOF spectra in principle contain sufficient information for an intrinsic absolute photon energy calibration if one peak can be identified. Since we have $L = 135 \pm 1$ mm and T is measured, the value E_K can be calculated. Fig. 3(a) presents a TOF spectrum for Ne 1s with binding energy $E_B = 870.2$ eV and natural linewidth 0.24 eV collected at photon energy $h\nu = 914$ eV. Data are summed over 100 pulses to improve statistics. The photon energy calibration of the SASE3 undulator gap has been performed over the entire photon energy range with the K-monochromator (Freund et al., 2019). At this photon energy, the cross section is $\sigma = 0.2$ Mb and the anisotropy parameter is $\beta = 2.00$. Peak center TOF is 34.25 ∓ 0.2 ns which from equation (1) leads to $E_K = 44.2 \pm 1.1$ eV. Adding the kinetic energy with

the binding energy gives the photon energy,

$$\underbrace{44.2\,\mathrm{eV}}_{E_K} + \underbrace{870.2\,\mathrm{eV}}_{E_B} \simeq \underbrace{914\,\mathrm{eV}}_{h\nu},$$

thus confirming that the undulator gap calibration is correct. In Fig. 3(a), the red curve shows kinetic energy as a function of TOF from equation (1). Furthermore, from the Ne 1s peak in Fig. 3(a) we estimate a spectral bandwidth of ~0.9% which is in excellent agreement with the bandwidth that we find from scanning over the monochromator and registering the intensity on an imager.

Fig. 3(b) presents TOF spectra at detector E for N₂ 1s with $E_B = 409.9$ eV and natural linewidth 0.115 eV at photon energies 899 eV, 904 eV and 914 eV. Data were also collected for many more photon energies up to 1000 eV. At these photon energies the cross section is $\sigma = 0.09$ Mb and the anisotropy parameter is $\beta = 2.00$. The retardation voltage was kept constant at −480 V. To provide pulse-resolved spectra, a mapping function must be constructed that converts TOF to kinetic energy for the applied retardation value R. In the situation of $R \neq 0$ due to field penetration in the drift-tubes, instead of equation (1) we derive a generalized expression,

$$E_K = P_R + \frac{P_L}{(T + P_T)^2}, \tag{2}$$

where P_R is a parameter that is related to the retardation voltage, P_L is related to drift-tube length and P_T is related to shift in TOF. The three parameters are characteristic for a certain value R and can be used to calculate E_K regardless of photon energy and target gas. Fig. 3(b) plots kinetic energy as a function of the TOF spectral peak mean value (black dots) for channel E. Equation (2) has been fitted to the data (red curve). The 16 individual drift-tubes have similar but non-identical parameters P_R, P_L and P_T which must be calculated for each of them. Fig. 3(b) furthermore demonstrates the PES energy resolution performance. The spectra at 899 eV and 904 eV overlap but have clearly distinguished mean values. We estimate that an energy difference of 1 eV can be separated. Therefore at this kinetic energy (~500 eV), neglecting the contribution of the SASE FEL bandwidth, we achieve a
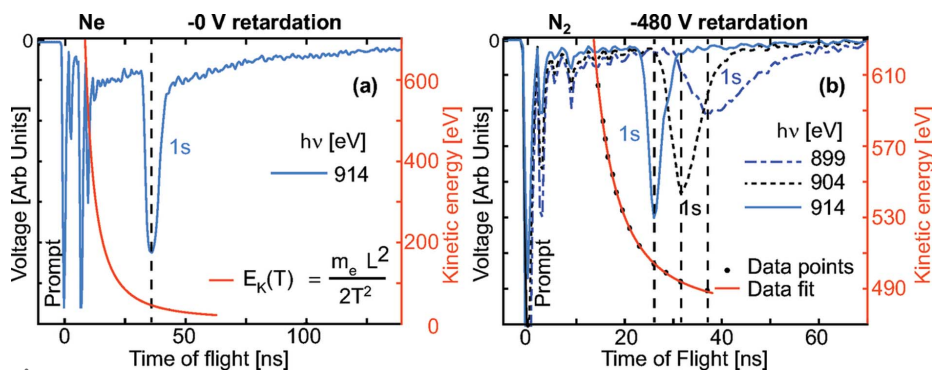
Figure 3
(a) 0 V retardation. Electron TOF spectrum after Ne 1s ionization at 914 eV. TOF is 36.25 ns which corresponds to a kinetic energy of 44.2 eV according to equation (1) (red curve). (b) −480 V retardation. Electron TOF spectrum after N₂ 1s ionization at different photon energies. Peak center (black dots) fitted to equation (2) (red curve). Spectra are averaged over 100 pulses for higher statistics.

research papers

kinetic energy resolution of $\sim 2 \times 10^{-3}$ which corresponds to $\sim 1 \times 10^{-3}$ photon energy resolution.

3.2. Polarimetry

Normalization of the 16 detector signals is accomplished with Auger lines whose intensity distribution is nearly isotropic in both polar and azimuth directions (Cleff & Mehlhorn, 1974). Auger lines can be isolated from the photoelectron lines by selecting suitable photon energy and drift-tube retardation. In particular the N_2 KVV transition energies in the range 357–367 eV (Cryan *et al.*, 2012) are useful for this purpose. Fig. 4 presents electron TOF data from an N_2 target with 867 eV photon energy and -340 V retardation voltage on eight of the channels. The data are summed over ten pulses for reliable statistics. The KVV peak is present at all channels with approximately constant intensity. The N_2 1s peak intensity, on the other hand, shows strong angular dependence which is expected due to the horizontal polarization and anisotropical distribution of this line ($\beta = 2.00$) at this photon energy. The peak identification has been confirmed by tuning the undulator gap and observing that the photo line is shifting proportionally to the photon energy while the KVV Auger band remains stationary. For background subtraction, we collected reference data files without gas injection but otherwise identical experimental conditions. After subtracting background we integrated the intensity of the KVV band on all 16 detectors and used these values for normalizing the individual detectors to correct for their non-identical performance.

We collected data for Ne 1s at 914 eV. Drift-tube voltages were set to 0 V. Fig. 5 presents intensity normalized TOF spectra from all 16 channels for a single-photon pulse. The first peak (red dashed) indicates scattered light which defines the start time. Photoelectron lines 2s and 2p and also the KLL Auger line (black dashed) have kinetic energies from 860 to 900 eV and a TOF around 20 ns which cannot be resolved with this retardation voltage. The Ne 1s photoelectron is highlighted in the gray region. We see that the relative signal intensity is highest in the horizontal plane E and W and close to zero in the vertical direction N and S. This indicates that the strongest component in the Stokes vector is the horizontal polarization with essentially no contribution from the vertical and also no unpolar-
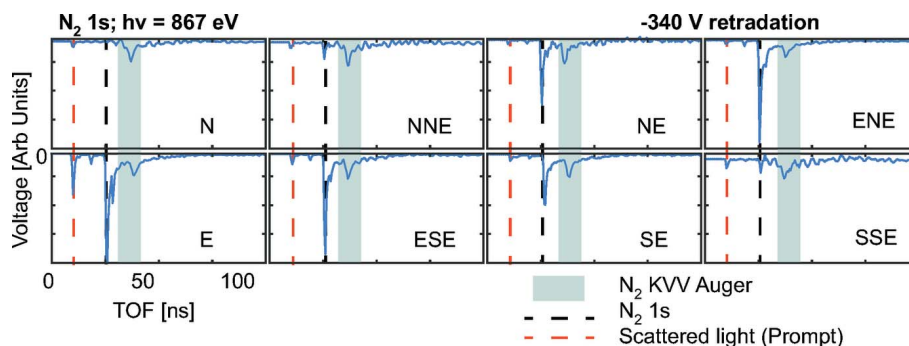
ized or circularly polarized light. When we study the intensity in all 16 detectors we obtain a picture of the photoelectrons angular distribution.

The red crosses in the polar plot in Fig. 6(a) represent the peak integrals over Ne 1s from one pulse after background subtraction. We have fitted to the data a polarization function P which describes the intensity as a function of the polar angle θ (Allaria *et al.*, 2014),

$$P(\theta) = 1 + \frac{\beta}{4}\left\{1 + 3P_{\mathrm{Lin}}\cos\left[2(\theta - \psi)\right]\right\}. \quad (3)$$

β is the anisotropy parameter, P_{Lin} is the linear polarization component and ψ is the tilt angle. For perfect horizontal polarization, we expect $P_{\mathrm{Lin}} = 1$ and $\psi = 0$. For this particular pulse we retrieved the values $P_{\mathrm{Lin}} = 0.96 \pm 0.03$ and $\psi =$

Figure 4
Electron TOF spectrum after N_2 ionization with $h\nu = 867$ eV and pulse energy ~ 234 µJ. Retardation voltage is -340 V. In all spectra we detect the KVV peak with approximately constant intensity, which makes this peak ideal for detector performance calibration. N_2 1s ($\beta = 2.00$), on the other hand, shows strong dependence on the polar axis.
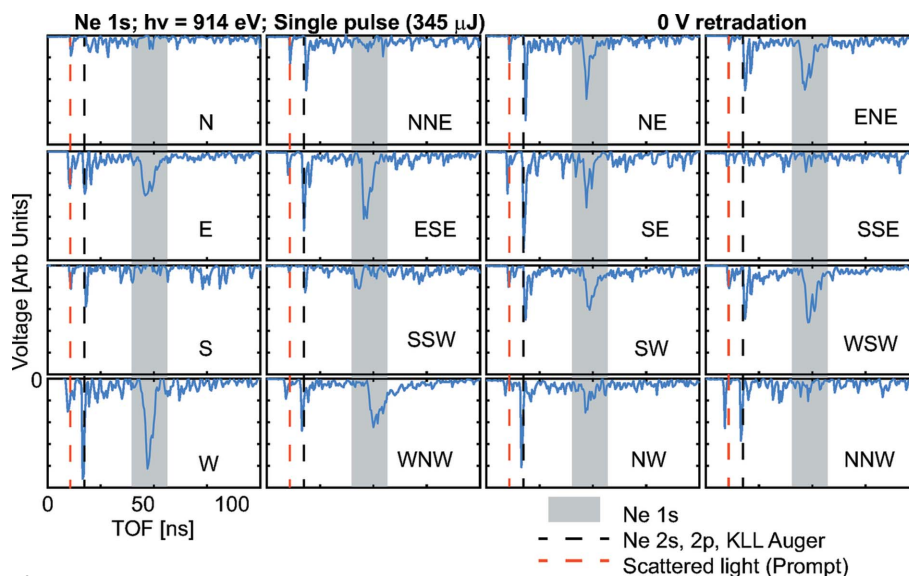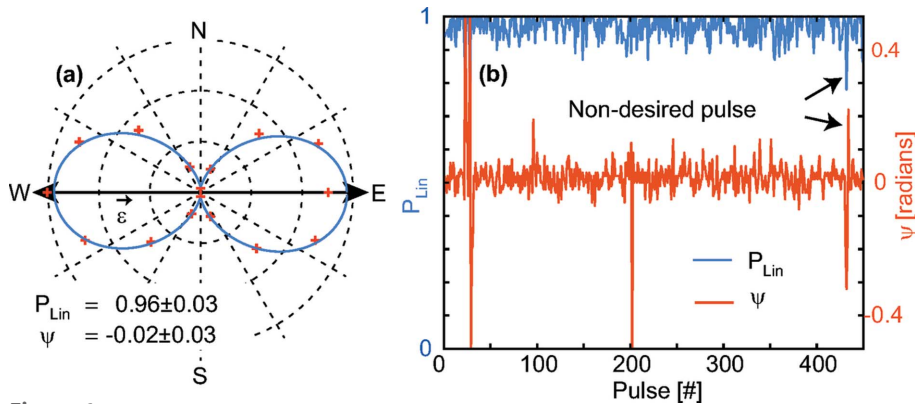
Figure 5
TOF spectra for Ne at $h\nu = 914$ eV with 16 electron TOF spectrometers oriented perpendicular with respect to the X-ray beam. The spectra are the result of one single pulse from the SASE3 undulator. Red dashed lines indicate scattered light which defines the start time. Black dashed lines indicate the photoelectron lines 2s and 2p and also KLL Auger lines. The gray area indicates the 1s peak. The Ne 1s photoelectron has $\beta = 2.00$. The intensity distribution is dominating in the horizontal plane E and W and close to zero in the vertical direction N and S which indicates that the strongest component in the Stokes vector is the horizontal polarization.

Figure 6
Polariziation data of individual XFEL pulses collected with Ne 1s at $h\nu = 914$ eV. (a) Polar plot representation of intensity data from one pulse with fitted parameters P_{Lin} and ψ from equation (3). The arrow indicates the polarization vector of light, $\boldsymbol{\varepsilon}$. (b) Polarization parameters for 450 consecutive pulses when the machine is operated in single-bunch mode. A few sharp spikes can be seen – these are pulses with undesired properties.

-0.02 ± 0.03. Error has been estimated as a 95% confidence interval of the fitting. The symbol $\boldsymbol{\varepsilon}$ indicates the polarization vector of X-rays. Note that this pulse-resolved technique is only capable of determining the linear polarization, in contrast to invasive multilayer-based polarimetery (Grizolli *et al.*, 2016) where the complete Stokes vector is found. However, for FELs, it is reasonable to assume only a negligible unpolarized contribution and that any deviation from linear polarization must be circular, either right-hand or left-hand polarized. A similar data set as presented in Fig. 6(a) was collected during single-bunch mode for a large amount of pulse trains. Fig. 6(b) presents P_{Lin} and ψ for 450 consecutive pulses, which characterizes the stability of the machine parameters.

3.3. Veto signal

Diagnostics-based generation of veto signals will significantly enhance the overall efficiency of the large pixelated imaging detectors at the scientific endstations, because it allows for real-time selection of pulse-resolved data. The PES in combination with the XGM will provide valuable input to the veto system.

In Fig. 6(b), sharp spikes can be seen for some pulses with values dramatically different from the expected interval. These data, that are usually related to too low pulse energy, inform us that this pulse has non-desired characteristics. This information could be fed into the veto system, preventing experiments from collecting data for this particular pulse.

4. Summary and outlook

We have installed the PES device in the SASE3 tunnel and integrated it in the EuXFEL control and data acquisition system. We have written algorithms that calculate spectral distribution and polarization from TOF spectra for soft X-ray photon diagnostics applications. The challenges that remain to be implemented are automatization with regard to voltage settings and gas selection in order for the device to operate unattended with minimal involvement from the users. Photon energy and polarization values must be provided in real time for both diagnostics and the veto system.

At present we are working on modifying the PES concept for the hard X-ray beamlines which imposes some additional challenges on the design criteria: for hard X-rays in the range 5–25 keV, resonances for the available gas targets are sparse (see Table 1) thus demanding the device to resolve high kinetic energy photoelectrons which requires longer drift-tubes and higher retardation voltages. In addition, cross sections are lower which we aim to compensate with larger detectors and a synchronized pulsed gas-injection capillary which leads to higher pressure in the interaction region at the time of the ionization.

References

Allaria, E., Diviacco, B., Callegari, C., Finetti, P., Mahieu, B., Viefhaus, J., Zangrando, M., De Ninno, G., Lambert, G., Ferrari, E., Buck, J., Ilchen, M., Vodungbo, B., Mahne, N., Svetina, C., Spezzani, C., Di Mitri, S., Penco, G., Trovó, M., Fawley, W. M., Rebernik, P. R., Gauthier, D., Grazioli, C., Coreno, M., Ressel, B., Kivimäki, A., Mazza, T., Glaser, L., Scholz, F., Seltmann, J., Gessler, P., Grünert, J., De Fanis, A., Meyer, M., Knie, A., Moeller, S. P., Raimondi, L., Capotondi, F., Pedersoli, E., Plekan, O., Danailov, M. B., Demidovich, A., Nikolov, I., Abrami, A., Gautier, J., Lüning, J., Zeitoun, P. & Giannessi, L. (2014). *Phys. Rev. X*, **4**, 041040.
Bostedt, C., Boutet, S., Fritz, D. M., Huang, Z., Lee, H. J., Lemke, H. T., Robert, A., Schlotter, W. F., Turner, J. J. & Williams, G. J. (2016). *Rev. Mod. Phys.* **88**, 015007.
Braune, M., Brenner, G., Dziarzhytski, S., Juranić, P., Sorokin, A. & Tiedtke, K. (2016). *J. Synchrotron Rad.* **23**, 10–20.
Braune, M., Buck, J., Kuhlmann, M., Grunewald, S., Düsterer, S., Viefhaus, J. & Tiedtke, K. (2018). *J. Synchrotron Rad.* **25**, 3–15.
Buck, J. (2012). *Conceptual Design Report: Online Time-of-Flight Photoemission Spectrometer for X-ray Photon Diagnostics.* Technical report XFEL.EU TR-2012–002). European XFEL, Hamburg, Germany.
Cardona, M. & Ley, L. (1978). *Photoemission in Solids I: General Principles.* Berlin: Springer-Verlag.

Cleff, B. & Mehlhorn, W. (1974). *J. Phys. B: At. Mol. Phys.* **7**, 593–604.

Cryan, P., Glownia, M., Andreasson, J., Belkacem, A., Berrah, N., Blaga, I., Bostedt, C., Bozek, J., Cherepkov, A., Dimauro, F., Fang, L., Gessner, O., Gühr, M., Hajdu, J., Hertlein, P., Hoener, M., Kornilov, O., Marangos, P., March, M., McFarland, K., Merdji, H., Messerschmidt, M., Petrovi, S., Raman, C., Ray, D., Reis, A., Semenov, K., Trigo, M., White, L., White, W., Young, L., Bucksbaum, H. & Coffee, N. (2012). *J. Phys. B At. Mol. Opt. Phys.* **45**, 055601.

Derevianko, A., Johnson, W. R. & Cheng, K. T. (1999). *At. Data Nucl. Data Tables*, **73**, 153–211.

Düsterer, S., Hartmann, G., Babies, F., Beckmann, A., Brenner, G., Buck, J., Costello, J., Dammann, L., Fanis, A. D., Geßler, P., Glaser, L., Ilchen, M., Johnsson, P., Kazansky, A. K., Kelly, T. J., Mazza, T., Meyer, M., Nosik, V. L., Sazhina, I. P., Scholz, F., Seltmann, J., Sotoudi, H., Viefhaus, J. & Kabachnik, N. M. (2016). *J. Phys. B At. Mol. Opt. Phys.* **49**, 165003.

Feldhaus, J., Krikunova, M., Meyer, M., Möller, T., Moshammer, R., Rudenko, A., Tschentscher, T. & Ullrich, J. (2013). *J. Phys. B At. Mol. Opt. Phys.* **46**, 164002.

Ferrari, E., Allaria, E., Buck, J., De Ninno, G., Diviacco, B., Gauthier, D., Giannessi, L., Glaser, L., Huang, Z., Ilchen, M., Lambert, G., Lutman, A. A., Mahieu, B., Penco, G., Spezzani, C. & Viefhaus, J. (2015). *Sci. Rep.* **5**, 13531.

Freund, W., Fröhlich, L., Karabekyan, S., Koch, A., Liu, J., Nölle, D., Wilgen, J. & Grünert, J. (2019). *J. Synchrotron Rad.* **26**, 1037–1044.

Grizolli, W., Laksman, J., Hennies, F., Jensen, B. N., Nyholm, R. & Sankari, R. (2016). *Rev. Sci. Instrum.* **87**, 025102.

Grünert, J., Planas Carbonell, M., Dietrich, F., Falk, T., Freund, W., Koch, A., Kujala, N., Laksman, J., Liu, J., Maltezopoulos, T., Tiedtke, K., Jastrow, U. F., Sorokin, A., Syresin, E., Grebentsov, A. & Brovko, O. (2019). *J. Synchrotron Rad.* **26**. To be published.

Hartmann, G., Lindahl, A. O., Knie, A., Hartmann, N., Lutman, A. A., MacArthur, J. P., Shevchuk, I., Buck, J., Galler, A., Glownia, J. M., Helml, W., Huang, Z., Kabachnik, N. M., Kazansky, A. K., Liu, J., Marinelli, A., Mazza, T., Nuhn, H. D., Walter, P., Viefhaus, J., Meyer, M., Moeller, S., Coffee, R. N. & Ilchen, M. (2016). *Rev. Sci. Instrum.* **87**, 083113.

Hartmann, N., Hartmann, G., Heider, R., Wagner, M. S., Ilchen, M., Buck, J., Lindahl, A. O., Benko, C., Grünert, J., Krzywinski, J., Liu, J., Lutman, A. A., Marinelli, A., Maxwell, T., Miahnahri, A. A., Moeller, S. P., Planas, M., Robinson, J., Kazansky, A. K., Kabachnik, N. M., Viefhaus, J., Feurer, T., Kienberger, R., Coffee, R. N. & Helml, W. (2018). *Nat. Photon.* **12**, 215–220.

Hauf, S. (2019). *J. Synchrotron Rad.* **26**. To be published.

Ilchen, M., Deinert, S., Glaser, L., Scholz, F., Seltmann, J., Walter, P. & Viefhaus, J. (2012). *J. Phys. B At. Mol. Opt. Phys.* **45**, 225102.

Ilchen, M., Hartmann, G., Gryzlova, E. V., Achner, A., Allaria, E., Beckmann, A., Braune, M., Buck, J., Callegari, C., Coffee, R. N., Cucini, R., Danailov, M., De Fanis, A., Demidovich, A., Ferrari, E., Finetti, P., Glaser, L., Knie, A., Lindahl, A. O., Plekan, O., Mahne, N., Mazza, T., Raimondi, L., Roussel, E., Scholz, F., Seltmann, J., Shevchuk, I., Svetina, C., Walter, P., Zangrando, M., Viefhaus, J., Grum-Grzhimailo, A. N. & Meyer, M. (2018). *Nat. Commun.* **9**, 4659.

Korff Schmising, C. von, Weder, D., Noll, T., Pfau, B., Hennecke, M., Strüber, C., Radu, I., Schneider, M., Staeck, S., Günther, C. M., Lüning, J., Merhe, A., Buck, J., Hartmann, G., Viefhaus, J., Treusch, R. & Eisebitt, S. (2017). *Rev. Sci. Instrum.* **88**, 053903.

Kraus, P. M., Zürch, M., Cushing, S. K., Neumark, D. M. & Leone, S. R. (2018). *Nat. Rev. Chem.* **2**, 82–94.

Lindle, D. W., Truesdale, C. M., Kobrin, P. H., Ferrett, T. A., Heimann, P. A., Becker, U., Kerkhoff, H. G. & Shirley, D. A. (1984). *J. Chem. Phys.* **81**, 5375–5378.

Lutman, A. A., MacArthur, J. P., Ilchen, M., Lindahl, A. O., Buck, J., Coffee, R. N., Dakovski, G. L., Dammann, L., Ding, Y., Dürr, H. A., Glaser, L., Grünert, J., Hartmann, G., Hartmann, N., Higley, D., Hirsch, K., Levashov, Y. I., Marinelli, A., Maxwell, T., Mitra, A., Moeller, S., Osipov, T., Peters, F., Planas, M., Shevchuk, I., Schlotter, W. F., Scholz, F., Seltmann, J., Viefhaus, J., Walter, P., Wolf, Z. R., Huang, Z. & Nuhn, H. D. (2016). *Nat. Photon.* **10**, 468–472.

Maltezopoulos, T., Laksman, J., Planas Carbonell, M., Dietrich, F., Liu, J., Freund, W., Koch, A., Jastrow, U. F., Sorokin, A., Tiedtke, K. & Grünert, J. (2019). *J. Synchrotron Rad.* **26**, 1045–1051.

Pellegrini, C., Marinelli, A. & Reiche, S. (2016). *Rev. Mod. Phys.* **88**, 015006.

Prince, K., Vondráček, M., Karvonen, J., Coreno, M., Camilloni, R., Avaldi, L. & de Simone, M. (1999). *J. Electron Spectrosc. Relat. Phenom.* **101–103**, 141–147.

Roussel, E., Allaria, E., Callegari, C., Coreno, M., Cucini, R., Mitri, S., Diviacco, B., Ferrari, E., Finetti, P., Gauthier, D., Penco, G., Raimondi, L., Svetina, C., Zangrando, M., Beckmann, A., Glaser, L., Hartmann, G., Scholz, F., Seltmann, J., Shevchuk, I., Viefhaus, J. & Giannessi, L. (2017). *Photonics*, **4**, 29.

Seddon, E. A., Clarke, J. A., Dunning, D. J., Masciovecchio, C., Milne, C. J., Parmigiani, F., Rugg, D., Spence, J. C. H., Thompson, N. R., Ueda, K., Vinko, S. M., Wark, J. S. & Wurth, W. (2017). *Rep. Prog. Phys.* **80**, 115901.

Tiedtke, K. E., Azima, A., von Bargen, N., Bittner, L., Bonfigt, S., Düsterer, S., Faatz, B., Frühling, U., Gensch, M., Gerth, C., Guerassimova, N., Hahn, U., Hans, T., Hesse, M., Honkavaar, K., Jastrow, U., Juranic, P., Kapitzki, S., Keitel, B., Kracht, T., Kuhlmann, M., Li, W. B., Martins, M., Núñez, T., Plönjes, E., Redlin, H., Saldin, E. L., Schneidmiller, E. A., Schneider, J. R., Schreiber, S., Stojanovic, N., Tavella, F., Toleikis, S., Treusch, R., Weigelt, H., Wellhöfer, M., Wabnitz, H., Yurkov, M. V. & Feldhaus, J. (2009). *New J. Phys.* **11**, 023029.

Tschentscher, T., Bressler, C., Grünert, J., Madsen, A., Mancuso, A. P., Meyer, M., Scherz, A., Sinn, H. & Zastrau, U. (2017). *Appl. Sci.* **7**, 592.

Ullrich, J., Rudenko, A. & Moshammer, R. (2012). *Annu. Rev. Phys. Chem.* **63**, 635–660.

Viefhaus, J., Scholz, F., Deinert, S., Glaser, L., Ilchen, M., Seltmann, J., Walter, P. & Siewert, F. (2013). *Nucl. Instrum. Methods Phys. Res. A*, **710**, 151–154.

Yabashi, M., Tanaka, H., Tanaka, T., Tomizawa, H., Togashi, T., Nagasono, M., Ishikawa, T., Harries, J. R., Hikosaka, Y., Hishikawa, A., Nagaya, K., Saito, N., Shigemasa, E., Yamanouchi, K. & Ueda, K. (2013). *J. Phys. B At. Mol. Opt. Phys.* **46**, 164001.

Yeh, J. & Lindau, I. (1985). *At. Data Nucl. Data Tables*, **32**, 1–155.